Photoconductivity and photovoltaic effect in indium selenide

A. Segura
Departamento de Electricidad y Magnetismo, Facultad de Ciencias Fisicas, Burjasot (Valencia), Spain
J. P. Guesdon and J. M. Besson[a)]
Laboratoire de Physique des Solides (Associé au CNRS), 4 Place Jussieu, Paris 5 eme, France
A. Chevy[a)]
Laboratoire de Luminescence II (Associé au CNRS), 4 Place Jussieu, Paris 5 eme, France

(Received 29 December 1981; accepted for publication 19 August 1982)

Transport and phototransport properties of crystalline indium monoselenide (InSe) doped with a variety of elements are reported. Measured mobilities, lifetimes, and effective diffusion lengths of photoexcited carriers are used to interpret electrical and photovoltaic properties of several different structures. These include *p-n* junctions, bismuth/*p*-type InSe, platinum/*n*-type InSe, and indium tin oxyde (ITO)/*p*-type InSe. External solar efficiencies of the best devices are between 5% and 6%. The influence on the efficiency of the various parameters is evaluated, and ways of improvement are discussed.

PACS numbers: 72.40. + w

I. INTRODUCTION

Indium monoselenide (InSe) belongs to the large class of layered semiconductors. In those crystals, a prototype of which is graphite, the molecular unit bonded by first-order covalent or ionic forces extends in two dimensions, instead of being three-dimensionally bonded as in group II-VI, IV, or III-V semiconductors. This bonding scheme is the key to the unique properties of layer compounds, which are radically different from those of more classical semiconductors as regards band structure, vibrational spectra, optical properties, or mechanical behavior. The knowledge of the aforementioned fundamental properties is a prerequisite to the interpretation of photoelectronic behavior. These properties of layered compounds have been investigated comparatively later than in other semiconductors. At the present time, nevertheless, relatively good data exist for this class of semiconductors, especially the Ga-In chalcogenides. In this series (GaS, GaSe, InSe), the elemental sheet is formed by pairs of graphite-like hexagonal lattices with two kinds of atoms. Two of these are bonded by metal-metal bridges which distort the hexagons. In its most common polytype, the rhombohedral one,[1] the elementary layer of InSe consists of three sheets, the rhombohedral axis normal to the layers being referred to, in this report, as the **c** axis.

Optical properties of InSe are well known in the ordinary configuration $\mathbf{E}\perp\mathbf{c}$ (Refs. 2–4) (**E** the electric vector of incident light) and partially for $\mathbf{E}\parallel\mathbf{c}$ (Refs. 3 and 5). Band structure calculations[6,7] and experimental data[8,9] assign to InSe a band scheme which is quite similar to the better-known compound GaSe. The valence and conduction band levels originate from a single layer which is then split by interlayer interaction. Carrier orbitals for those levels thus extend along the **c** axis, and therefore have little two-dimensional character. A consequence is that effective masses do not exhibit large anisotropies. In some cases in the In, Ga chalcogenides, effective masses along **c** may be *smaller* than within the layers.[10] The large anisotropies found in transport properties are partly or wholly assignable to interlayer macroscopic defects and/or planes of precipitates.[11–15]

The energy gap in InSe is "quasi-direct." The direct gap is at 1.3 eV at 300 K, and the optical transition is only weakly allowed by spin-orbit coupling for $\mathbf{E}\perp\mathbf{c}$, which is by far the most accessible configuration for experiment. Thus, in contrast with other direct-gap semiconductors, the absorption coefficient $\alpha_\perp$ (Refs. 2–4) is only 10^3 cm^{-1} at the absorption edge, instead of 10^4–10^5 cm^{-1}, as in GaAs or CdS, for instance. This is an important factor for solar energy conversion, and optimal geometries of InSe solar cells are completely different from those of GaAs, CdS, or silicon. The indirect gap, some 50 meV below the energy of the direct gap, is weak enough not to be observable in optical absorption. Its presence is nevertheless certainly the reason for the high lifetimes and diffusion lengths of photoexcited carriers.

Transport properties and the conductivity anisotropy have been studied by several authors[16,17] who had noted the large difference in apparent mobilities μ along the **c** axis and in the layers ($\mu_\perp/\mu_\parallel \sim 10^2$). The remarkable photoconductivity behavior, with the occurrence in InSe of negative photoconductivity and photomemory effects,[18–20] has led to propose complex schemes of recombination centers. Photovoltaic properties have been studied in a few papers,[21–29] mostly on crystalline material; although attempts have been made to fabricate devices from vacuum-deposited layers of nonstoichiometric In_xSe_{1-x}.[30,31] This was a natural step since InSe stands out for its attractive potentialities for solar energy photovoltaic conversion,[32] as evidenced by the following:

(i) its energy gap (1.3 eV) is close to the solar optimum;

(ii) mobilities over 1000 cm^2/V sec in the layer plane can be obtained;

(iii) diffusion lengths are over 1 mm in the layer plane and 5 μm across the layers, even in comparatively low-purity material;

(iv) natural, as-cleaved surfaces have quasi-perfect optical quality, and free first-order bonds being absent, they are

[a)] Present address: Laboratoire de Physique des Milieux très Condensés (associé au C.N.R.S.) 4 place Jussieu 75230 PARIS Cédex 05-France.

 0021-8979/83/020876-13$02.40

not subject to adsorption.

Apart from these practical considerations, InSe is an attractive system as a model for the study of anisotropic transport and phototransport properties. Its two-dimensional behavior makes bulk InSe analogous in many respects to surface regions in three-dimensional semiconductors.[33] In this paper, we present a summary of our work on the photoelectronic parameters of InSe and their influence on the behavior of several types of devices for photovoltaic conversion, a few of which had already been briefly reported before.

Transport and material properties are examined in Sec. III, photoconductivity and fundamental photovoltaic parameters in Secs. IV and V. In Sec. VI, quantitative fits to the observed spectra of the junctions are given. Solar efficiencies are then reported and discussed.

II. EXPERIMENTAL

Crystals are grown by the Bridgman method from a nonstoichiometric melt.[1] Doping agents used here to obtain *n*- and *p*-type material (Cl,Cd,Zn,As,Ga,S) are introduced into the polycrystalline powder, as compounds such as InAs, InS, GaSe, and GaS. Samples are prepared by cleaving from the ingot with a razor blade. Slabs down to a few microns in thickness and 20 mm^2 in area can be prepared by this method.

Ohmic contacts are made by In evaporation and are annealed at 200 °C under argon gas. Such contacts are ohmic at room temperature for low voltages. At liquid N_2 temperature, their behavior is erratic and, on some samples, they become rectifying, while on others, they remain ohmic. Only the latter are quoted for low-temperature data in Table I.

TABLE I. Hall effect measurements on materials referred to in the text. *Column 2*: Concentrations of doping agents refer to quantities introduced into the melt, except for 554/116 material where Ga, S, and Na were the most abundant impurities found in the monocrystal by mass spectrography. Absence of mention indicates unintentionally doped material. *Column 4 and 5*: Hall currents and voltages in the plane of the layer (cleaved samples). *Column 6*: Apparent carrier density from Hall effect.

1	2	3	4	5	6	7
Reference crystal *n*°	Doping agent	Type	ρ (Ω, cm)	μ_H (cm^2/V sec)	Carrier density (cm^{-3})	Remarks
364/11	...	*N*	6.6	500	2×10^{15}	...
382/21	...	*N*	16.0	310	10^{15}	...
357/6	...	*N*	8.6	700	10^{15}	...
554/116	Ga: 8 ppm S: 10 ppm Na: 10 ppm	*N*	770	20	4×10^{14}	4N In metal Doping agent found by analysis.
493/69	$InCl_3$: 10 ppm	*N*	1	520	10^{16}	...
id.	id.	*N*	0.25	4500	6×10^{15}	77 K
id.	id.	*N*	0.15	730	6×10^{16}	500 °C annealed
id.	id.	*N*	0.05	7600	2×10^{16}	77 K
618/172	GaS: 15 ppm	*N*	0.65	980	10^{16}	...
626/180	GaSe: 130 ppm	*N*	5.4	790	2×10^{15}	...
674/208	InS: 2 ppm	*N*	1.5	710	6×10^{15}	...
393/23	ZnSe: 1000 ppm	*P*	1100	90	6×10^{13}	...
id.	id.	*N*	0.2	80	4×10^{17}	500 °C annealed
476/61	ZnSe: 1%	*P*	180	8	4×10^{15}	...
id.	id.	*N*	9.5	20	4×10^{16}	500 °C annealed
507/81	CdSe: 1%	*P*	200	15	2×10^{15}	...
id.	id.	*N*	0.6	30	4×10^{17}	500 °C annealed
524/94	InAs: 1 ppm	*P*	230	9	3×10^{15}	...
537/102	InP: 1000 ppm	*P*	880	30	2×10^{14}	...
561/122	ZnSe: 1000 ppm	*P*	310	40	5×10^{14}	...

Hall effect was measured only in the layer plane since the structure of InSe precludes its being sawn or cleaved parallel to the **c** axis without considerable damage. Resistivity was measured for transit directions parallel and perpendicular to the **c** axis.

Electrical characteristics $J(V)$ are measured with a Tektronix 575 curve tracer. Capacitance measurements are done on an ESI 290-A bridge at a frequency of 1 kHz. Photovoltage and photoconductivity spectra are recorded using a Jobin Yvon H20 infrared (IR) monochromator. Spectral bandwidth varies between 40 and 8 Å. The source is a halogen burner with 3000 K radiation temperature. The beam is chopped at a frequency of 800 Hz by a PAR 125-A modulator and amplified with a PAR 128-A lock-in. All spectra in this paper are at constant incident photon flux with the photovoltaic response being corrected against the known absolute response of a PbS cell. Solar efficiencies were measured either under natural illumination or under simulated AM1 flux, and calibrated against a standard silicon cell.

III. TRANSPORT PROPERTIES

Table I shows the results of Hall effect measurements for a selection of n- and p-type samples. Considerable dispersion of the results is usually found even on samples from the same ingot, which points to inhomogeneity of the material. Thus we give in Table I average values for mobilities in the layer plane and for carrier concentrations. Nevertheless, the values we observe in n-type samples (between 100 and 1000 cm^2/V sec at 300 K) are similar to those of "classical" semiconductors for carrier concentrations of 10^{15}–10^{16} cm^{-3}; although in InSe, the impurity concentration may be much higher. The apparent carrier concentration, as measured by Hall effect on p-type samples, is lower than 5×10^{15} cm^{-3}. The low-temperature behavior indicates large compensation since those p-type samples become n-type at 77 K, with low mobilities. Thus, the apparent mobilities and carrier densities observed by Hall effect will be regarded here only as a qualitative characterization of the samples. In any case on average, mobilities in p-type samples are over one order of magnitude lower than in n-type samples (Table I). This is expected in view of the high-impurity concentration in the starting material (up to 10^{20} cm^{-3}) for the p-type samples. Annealing of p-type (Zn-doped) material at 500 °C makes it revert to n-type, which shows that the p-type character is a metastable property of the crystal. Nevertheless, as shown in Sec. VI, this property can be utilized to prepare p-n junctions by a thermal process. Finally, in all samples, the transport (conductivity) anisotropy with respect to the **c** axis is of the order of 10^2 or more in accordance with previous work.[16,17]

The dependence of transport properties upon the band structure is less than clear in layer compounds. In the case of InSe, electron mobilities $\mu_\perp$ in n-type material are ten times higher than hole mobilities in p-type samples, and this can be ascribed to effective masses perpendicular to the **c** axis being[8] $0.15m_0$ for electrons and $1.0m_0$ for holes. Nevertheless, the effective mass anisotropy $m_\parallel/m_\perp$ is 1 for electrons, and from 2 to 3 for holes. This is completely different from the observed conductivity anisotropy, which is in the range of a few 10^2. Thus, in view of the very high impurity content of all samples, transport properties are evidently dominated by the influence of stacking faults and highly anisotropic scattering mechanisms (interlayer defects), and not by intrinsic band structure properties, at least in the comparatively impure samples used. Therefore, little can be said about the nature and site of impurity levels or their position with respect to the bands.

Nevertheless, in some cases, the influence of doping agents can be understood.

(i) The p-type character of column II elements (Cd,Zn) can be explained by substitution of one atom to one indium pair. These elements tend to form layered compounds with halogens (e.g., CdI_2,ZnI_2). Thus, a layered configuration with binding to column VI elements leads to an electron deficit and to p-type character. This view is supported by the fact that Pb, which also forms a layer crystal (PbI_2) with the CdI_2 structure, also dopes InSe p-type; although, it is a column IV element.

(ii) Column V elements (As,P) are p-type dopants by substitution for selenium. By the same process, halogens (Cl,I) are reliable n-type dopants. The behavior of unintentionally doped samples made from high-purity (6N) elements or isoelectronically doped samples (e.g., doped with GaS) is more difficult to understand; they consistently come out as n-type. This might be due to an excess of In in the highly nonstoichiometric starting material ($In_{1.12}Se_{0.88}$).

IV. PHOTOCONDUCTIVITY

Photoconductive devices were used to obtain the transport parameters of photogenerated carriers. Three types of experiments are reported here.

(i) Time response of the photoconductivity signal perpendicular and parallel to **c** (Fig. 1).

(ii) Traveling spot method to measure the diffusion length in the layers $L_\perp$.

(iii) Photoconductivity spectra fitted to the diffusion length across the layer $L_\parallel$.

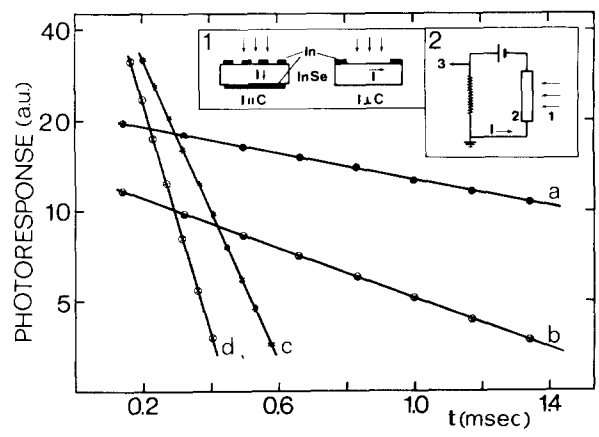

FIG. 1. Photoconductivity decay time at 300 K. All figures in the paper refer to 300 K, except when otherwise indicated. Photoconductivity (log scale) in response to a 20-μsec light pulse. Insert 1: Geometries used in the experiment. $\mathbf{I}_\parallel\mathbf{c}$ and $\mathbf{I}_\perp\mathbf{c}$: photoexcited carriers drift parallel and perpendicular to the **c** axis. Insert 2: Experimental setup: Light pulse (1) incident on sample (2) generates photoconductive signal on oscilloscope (3). Curve a: n-type sample (364/11), $I_\perp\mathbf{c}$, $\tau_{n\perp}$ = 1.5 msec, Curve b: p-type sample (393/23), $I_\perp\mathbf{c}$, $\tau_{p\perp}$ = 0.7 msec, Curve c: n-type sample (364/11), $I_\parallel\mathbf{c}$, $\tau_{n\parallel}$ = 0.17 msec, Curve d: p-type sample (393/23), $I_\parallel\mathbf{c}$, $\tau_{p\parallel}$ = 0.10 msec.

TABLE II. Typical transport parameters for InSe. Errors given refer to the spread of values from sample to sample, not to the measurements, which have negligible experimental error. *Column 2*: Hall effect mobilities for *n*-type unannealed samples. *Column 3*: Photoexcited carriers lifetime, from the time decay of photoconductivity (Fig. 1), for carrier drift along the layer plane. *Column 4*: Diffusion length of carriers along the layers $L_{\perp\,\mathrm{calc}} = (kT\mu_\perp\tau_\perp/q)^{1/2}$. $\mu_\perp$ and $\tau_\perp$ from columns 2 and 3. *Column 5*: Diffusion length in the layer plane measured by the travelling spot method. *Column 6*: Carrier mobility for transport along the c axis, $\mu_\parallel = \mu_\perp(\rho_\perp/\rho_\parallel)$. Resistivities $\rho_\parallel$ and $\rho_\perp$ have been measured on cleaved samples. $\mu_\perp$ from Table I. *Column 7*: Lifetime of photoexcited carriers from the time decay of photoconductivity, for carrier drift along the c axis. *Column 8*: Diffusion length of carriers along the c axis, $L_{\parallel\,\mathrm{calc}} = (kT\mu_\parallel\tau_\parallel/q)^{1/2}$. $\mu_\parallel$ and $\tau_\parallel$ from columns 6 and 7.

1	2	3	4	5	6	7	8	9
Type	$\mu_{H\perp}$ cm^2/V sec	$\tau_\perp$ msec	$L_{\perp\,\mathrm{calc}}$ mm	$L_{\perp\,\mathrm{meas}}$ mm	$\mu_\parallel$ cm^2/V sec	$\tau_\parallel$ msec	$L_{\parallel\,\mathrm{calc}}$ μm	$L_{\parallel\,\mathrm{meas}}$ μm
N	600 ± 300	1.5 ± 0.5	1.5 ± 0.5	1 ± 0.5	2 ± 1	0.17 ± 0.04	29 ± 10	20 to 30
P	10 to 90	0.2 to 0.7	0.2 to 0.4	0.4 ± 0.1	0.2 ± 0.1	0.1 ± 0.05	7 ± 4	...

The experimental setup to measure the effective lifetime of photogenerated carriers is shown in the insert of Fig. 1. The photoconductivity response to light pulses 20 μsec in length is directly observed on an oscilloscope and plotted on a semilog scale with respect to time.

The photoconductivity voltage is

$$\Delta V \propto \exp(-t/\tau), \tag{1}$$

and the characteristic lifetimes for carrier drifts parallel $\tau_\parallel$ and perpendicular ($\tau_\perp$) to the **c** axis are given in Table II (columns 3 and 7). Lifetime $\tau_\perp$ was measured with the electrodes on the same side of the illuminated sample, which was cleaved perpendicular to the **c** axis. Lifetime $\tau_\parallel$ was measured with electrodes at the front and at the back of the sample. The values given here for *n*-type samples are typical for this type of material.

In *p*-type material, lifetimes were in some cases shorter than 20 μsec and could not be measured by this method. Therefore, for *p*-type material, only lifetimes longer than 20 μsec are given in Table II. In *p*-type samples, lifetimes take different values from sample to sample; although they are, on average, an order of magnitude smaller than in *n*-type material. Also, the lifetime as measured by this method comes out as an anisotropic quantity with $\tau_\perp/\tau_\parallel$ as high as 20. This would not make sense in an isotropic semiconductor where lifetimes have to be scalar quantities. In the case of layer compounds, where interlayer macroscopic defects exist (two-dimensional precipitates and/or stacking faults), this "anisotropy" of phenomenological lifetimes simply represents a difference in scattering processes for carriers propagating perpendicular to **c** in the quasi-perfect crystal between defects, and for carriers which propagate parallel to **c** and have to go through the extended two-dimensional defect planes parallel to the layers.[12,13]

Diffusion lengths parallel to the layers $L_\perp$ were measured by the traveling spot method (Fig. 2, insert). The dependence of the conductivity voltage ΔV on the distance x between the light spot and the current electrodes is

$$\Delta V \propto \exp(-x/L_\perp). \tag{2}$$

Values of $L_\perp$ given in Table II (column 5) are taken from the slope of the right-hand part of the plot in Fig. 2. A remarkable behavior of *p*-type samples in that respect is that although they revert from *p*-type to *n*-type under annealing, as mentioned in the preceding section, $L_\perp$, as measured by this method, does not vary. This shows that the ambipolar diffusion length of carriers along the layers is only weakly dependent on the nature of interlayer defects. Although the crystal as a whole may contain a large number of defects, the space between those defects acts like a quasi-perfect two-dimensional sample where photogenerated carriers may have comparatively large lifetimes when not forced to cross defect sites or precipitates.

The photoconductivity spectrum was measured with electrodes on the front (illuminated) or back surfaces (Figs. 3 and 4). In Fig. 3, two representative spectra are shown at 300 and 90 K, for constant photon flux. The dashed lines are calculated values for the photoconductivity signal ΔV with

$$\Delta V \propto 1 - \exp(-\alpha d), \tag{3}$$

where α is the absorption coefficient of InSe (Refs. 2 and 3), and d is the thickness of the sample. The fit is good up to 2.6 eV, where surface effects decrease the carrier lifetime.

The geometry shown in the insert of Fig. 4 has been used to obtain a value of $L_\parallel$, using samples of different thicknesses d. In InSe, the conductivity in the layer plane is orders

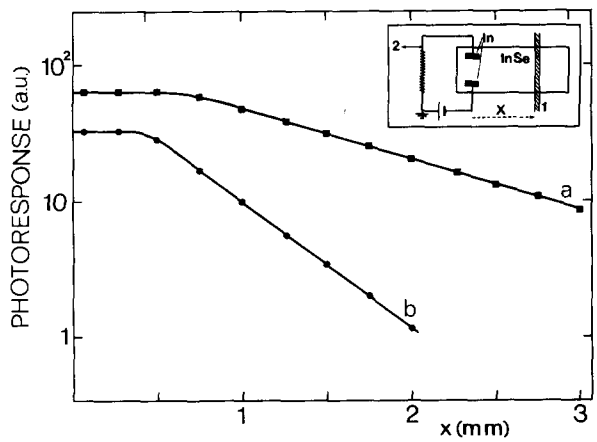

FIG. 2. Measurement of the diffusion length L by the traveling spot method. Insert: Schematic layout. **c** axis is perpendicular to the diagram. White light spot (1) is x mm away from the electrodes for photoconductivity measurements. Photoconductivity signal (2) in response to a light signal modulated at 400 Hz. Curve a: Photoresponse (log scale) of an *n*-type sample (364/11). Slope corresponds to $L_{n\perp} = 1 \pm 0.5$ mm. Curve b: same for *p*-type sample (393/23). $L_{p\perp} = 0.4 \pm 0.1$ mm.

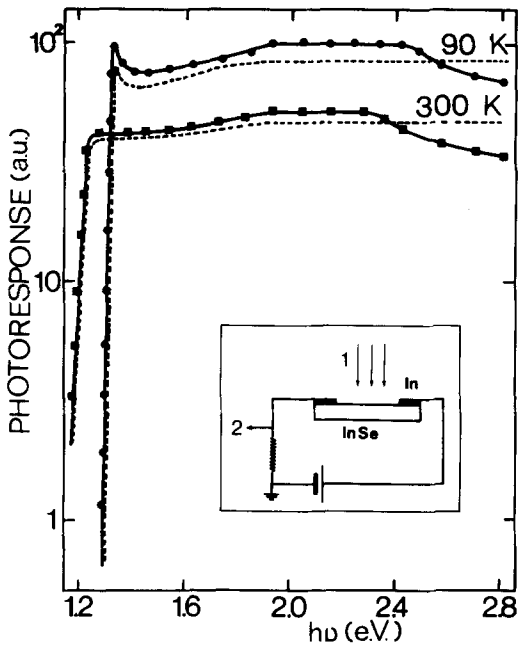

FIG. 3. Full lines: photoconductivity (log scale), for carrier drift parallel to the layer, versus incident photon energy, for n-type material (364/11), under constant photon flux at two temperatures. Front illumination (insert). Dashed curves: spectra calculated with Eq. (3) for the thickness of this sample ($d = 21\ \mu$m).

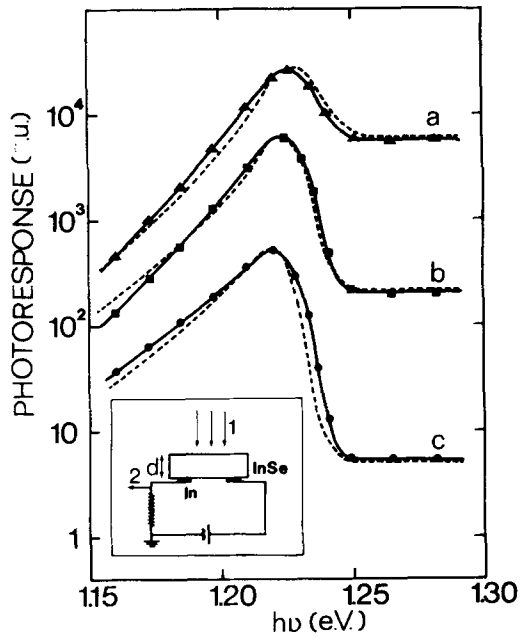

FIG. 4. Full lines: photoconductivity spectrum (log scale), for carrier drift parallel to the layer, for n-type InSe (382/21). Constant photon flux parallel to c. Back illumination (insert). Sample thicknesses d are: curve a, 80 μm; curve b, 130 μm; curve c, 230 μm. Dashed curves are fits along Eq. (4) for those thickness with $L_{\parallel} = 20 \pm 3\ \mu$m for (a) and (b), $L_{\parallel} = 30 \pm 4\ \mu$m for (c).

of magnitude larger than in the direction of the c axis. Thus the current lines between the two bottom electrodes do not extend far into the bulk of the crystal, but remain concentrated close to the bottom surface at a distance which is much smaller than the sample thickness. Thus the photoconductivity signal only depends upon the photogenerated carrier concentration near the bottom surface, which is given by

$$\Delta V \propto \frac{\alpha^2 L_{\parallel}^2}{\alpha^2 L_{\parallel}^2 - 1}\left[\exp(-d/L_{\parallel}) - \frac{1}{\alpha L_{\parallel}}\exp(-\alpha d)\right], \tag{4}$$

with $L_{\parallel}$ the effective (ambipolar) diffusion length. This equation is derived from diffusion equations [Eq. (6) in Sec. V] with limiting conditions: $(\partial p/\partial x)_{x=0} = 0$ (zero surface recombination) and $p \to p_0$ for $x \to \infty$ (diffusion length is small with respect to sample thickness).

In Fig. 4, a fit of Eq. (4) with experimental data is given for three thicknesses. The difference in phenomenological diffusion lengths used in this fit reflects the influence of surface layers, which decreases the average diffusion lengths. This effect, as expected, is more important in the thinner samples.

In Fig. 3, the decay of the photoconductivity voltage above 2.4 eV (i.e., for absorption coefficients $\alpha_{\perp} > 20\,000$ cm^{-1}) is readily visible. This effect reveals the existence of a perturbed surface layer which must be of the order of 0.5 μm since it comes in for penetration depths of light of $\sim 0.5\ \mu$m ($\alpha = 2 \times 10^4$ cm^{-1}). Optical measurements[3] on other layer compounds of the same family have shown the existence of such perturbed layers induced by cleaving or mechanical damage.

In Table II, the values given for L were verified by calculating diffusion lengths from the usual formula:

$$L = [(kT\mu\tau)/q]^{1/2}, \tag{5}$$

where L is the diffusion length; k is the Boltzmann constant; T is the temperature; q is the electron charge; μ is the mobility, and τ is the lifetime.

The theoretical values are given in columns 4 and 8. Measured and calculated values for $L_{\perp}$ and $L_{\parallel}$ fit best for n-type material, compared to p-type material. For low-lifetime p-type material ($\tau_{\perp} \sim 0.2$ msec), mobilities calculated from $L_{\perp}$ and $\tau_{\perp}$ would be several hundred cm^2/V sec, which is comparable to n-type material. Actual Hall mobilities are much lower (Table I). One explanation may be that, for p-type material, the Hall mobility is determined by that of majority carriers (holes).

The photoconductive effective mobility is only limited by that of photoexcited minority carriers (electrons), since the method used here for $L_{\perp}$ is sensitive to carriers with the higher diffusion length (in this case, electrons). A second explanation comes from the fact that the p-type InSe which is used here is an extreme case of impurity segregation in layer compounds. Although up to 1% Zn has been introduced into the melt and identified afterwards by quantitative analysis, the apparent carrier concentration remains lower than 10^{16} cm^{-3}. This indicates that the sample is made up of slightly doped regions, separated by two-dimensional macroscopic precipitates of the doping agent perpendicular to the c axis. This is consistent with other evidence[33] and explains why (e.g., sample 393/23, Table I) mobilities along the layer of the order of 100 cm^2/V sec can still be observed with material containing, as a whole, 1000 ppm impurities. Be-

cause of this structure, lifetimes derived by standard formulae such as Eq. (5) appear as a tensor and not as a scalar quantity. Transport along the **c** axis is dominated by the planar defects potential wells, which act as series resistances. On the contrary, transport along the layer, perpendicular to **c**, is mostly dependent upon the properties of the quasi-perfect material between the defects and thus the classical three-dimensional treatment of diffusion does not really apply here. Transport parameters ($L_{\parallel}$ or $\tau_{\parallel}$) along the **c** axis are thus given here only as phenomenological quantities for comparison with the same quantities in three-dimensional semiconductors. As will be shown in the next sections, even with those restrictions, the effective diffusion length across the layers remains a meaningful parameter to interpret photovoltaic spectra in a quantitative fashion.

V. PHOTOVOLTAIC EFFECT

In this section, basic parameters of the photovoltaic process are studied. Diffusion equations used in this section and the next one are established and applied to the interpretation of the photovoltaic spectra of experimental structures. The structures are specifically made to measure the diffusion lengths of minority photoexcited carriers in the material used for the devices (Sec. VI).

For a sample with homogeneous illumination normal to the layers, the one-dimensional diffusion equation along the **c** axis, for a given type of carrier (e.g., for holes) is

$$D\frac{\partial^2 p}{\partial x^2}-\frac{p-p_0}{\tau}=-\alpha\Phi_0\exp(-\alpha x)\,, \tag{6}$$

where D is the diffusion coefficient of photogenerated carriers; τ is the lifetime coefficient of photogenerated carriers; α is the absorption coefficient of the material; Φ_0 is the photon flux density; p is the hole density, and p_0 is the equilibrium hole density. The general solution for current density is

$$J=A\exp(x/L)+B\exp(-x/L)+q\frac{\Phi_0\alpha^2\exp(-\alpha x)}{\alpha^2-1/D\tau}\,, \tag{7}$$

where $L=(D\tau)^{1/2}$ and A and B are constants.

In the case of a p-n junction of total thickness e at a distance d from the n-type illuminated surface, with an effective depletion width w, the three contributions to the photocurrent must be taken into account. Here, p and n are the hole and electron densities, or, as indices, refer to quantities related to holes or electrons.

(i) Hole current in the front n-type region.

Limiting conditions are

$\left(\frac{\partial p}{\partial x}\right)_{x=0}=0$, zero surface recombination rate at the front surface.

$(p)_{x=d}=p_0$, no excess minority carriers at the barrier edge.

The exact solution is

$$J_p=q\Phi_0\frac{\alpha^2L_p^2}{\alpha^2L_p^2-1}\left[\frac{1}{\cosh(d/L_p)}-\frac{1}{\alpha L_p}\exp(-\alpha d)\left(1+\tanh\frac{d}{L_p}\right)\right]. \tag{8}$$

A simple form can be derived only by integrating the number of photoexcited carriers which reach the junction[34]:

$$J_p=q\Phi_0\frac{\alpha L_p}{\alpha L_p-1}\left[\exp(-d/L_p)-\exp(-\alpha d)\right]. \tag{9}$$

Throughout this paper, it is understood that experimental values of photocurrents or photovoltages are corrected for reflectivity losses, and that small Fabry-Perot interference fringes are smoothed out by taking an average value. Also, making use of Eq. (9) yields fitting parameters which coincide with those obtained from Eq. (8) within 20%, which is smaller than the dispersion among devices from the same batch. For this reason we used the latter, which, although less accurate, still gives sufficient accuracy for our purpose.

(ii) Contribution from the depletion layer.

All photogenerated carriers are assumed to participate in the photovoltaic process and their contribution is thus

$$J_d=q\Phi_0\exp(-\alpha d)[1-\exp(-\alpha w)]\,. \tag{10}$$

(iii) Contribution of the p-type base (electron current). Here, limiting conditions are

$(n)_{x=d+w}=n_0$: zero excess minority carriers at the barrier edge.

$\left(\frac{\partial n}{\partial x}\right)_{x=e}=0$: no surface recombination at the bottom surface.

The electron contribution is

$$J_n=q\Phi_0\frac{\alpha^2L_n^2}{\alpha^2L_n^2-1}\exp(-\alpha d-\alpha w)\times\left[\frac{1-(1/\alpha L_n)\sinh(e/L_n)}{\cosh\frac{e-d-w}{L_n}}+1\right]. \tag{11}$$

For $e\gg d+w$ and $e\gg L_n$, this reduces to

$$J_n=q\Phi_0\frac{\alpha L_n}{\alpha L_n+1}\exp(-\alpha d-\alpha w)\,. \tag{12}$$

The case of a Schottky junction can be treated as a particular case with $d=0$. The total current [Eqs. (10) and (12)] is then

$$J_{\rm Sch}=q\Phi_0\left[1-\exp(-\alpha w)+\frac{\alpha L_n}{\alpha L_n+1}\exp(-\alpha w)\right]. \tag{13}$$

Surface effects are taken into account by introducing a perturbed surface layer of thickness δ, where the lifetime of photoexcited carriers is small enough that their contribution to the photocurrent can be neglected. Equation (9) is then transformed into:

$$J_p=q\Phi_0\frac{\alpha L_p}{\alpha L_p-1}\times\left[\exp(-\alpha\delta)\exp\left(-\frac{d-\delta}{L_p}\right)-\exp(-\alpha d)\right], \tag{14}$$

and Eq. (13) becomes

$$J_{\rm Sch}=q\Phi_0\left[\exp(-\alpha\delta)-\frac{1}{\alpha L_n+1}\exp(-\alpha w)\right]. \tag{15}$$

Another model which we used to describe surface effects was to use an exponential increase of the effective lifetime of photogenerated carriers, away from the surface, instead of an abrupt variation. This was accounted for by expressing the equivalent quantum efficiency as $[1 - \exp(-x/\delta)]$. Equation (9) becomes

$$J_p = q\Phi_0 \left\{ \frac{\alpha^2 L_p^2}{\alpha^2 L_p^2 - 1} \left[\exp(-d/L_p) - \exp(-\alpha d) \right] - \frac{\alpha\left(\alpha - \frac{1}{\delta}\right) L_p^2}{\left(\alpha - \frac{1}{\delta}\right)^2 L_p^2 - 1} \left[\exp(-d/L_p) - \exp\left(-\alpha d - \frac{d}{\delta}\right) \right] \right\}. \tag{16}$$

In Eqs. (6)–(16), ϕ_0 the incident flux, is the number of photons which penetrate into the material per unit area and per second; that is, after corrections for reflectivity losses which are computed from the known values of the refractive index.[3]

Experimental, weakly rectifying structures have been made to measure $L_\parallel$, as shown in Figs. 5 and 6. One or two small annealed indium contacts (ohmic) are placed close to a large unannealed (rectifying) indium contact at the back (unilluminated) surface of the sample. Small as the potential barrier may be, it is sufficient to collect photoexcited carriers which reach the junction, and to give an accurate spectrum of the *relative* spectral response of the bulk material. On Fig. 5 are shown the spectra of a 13-micron n-type slab (357/6) at 300 K and 90 K (full curves). Fits along Eq. (9) are shown as dashed curves with $L_\parallel = 5$ microns at 300 K and $L_\parallel = 25$ microns at 90 K. The fit is reasonable even at low temperature at the exciton peak and in the high-energy region, where penetration lengths of light are smaller than 1 micron. This indicates, for this sample, little perturbation from surface damage.

The behavior shown in Fig. 6 is rather different. For this p-type material (476/61), room-temperature spectra could be fitted with Eq. (9), with two different thicknesses and diffusion lengths ($L_\parallel = 1$ micron for the thinner sample and $L_\parallel = 1.7$ microns for the thicker one) without introducing a damaged surface layer. This difference in effective diffusion lengths between the two samples at least partly represents a perturbed surface layer which is more important on the thinner sample, but still can be accounted for by using different values of $L_\parallel$ in Eq. (9). On the contrary, at low temperatures (spectra c and d on Fig. 6), the diffusion length of the bulk material is so large that surface effects strongly modify the spectrum in the high-energy region, and no fit is possible with Eq. (9). Using now Eq. (16) which takes into account a surface layer, a fit is possible (caption to Fig. 6). In this case, however, no fit is possible in the exciton region (around 1.3 eV). Here the dashed line has been computed with the absorption coefficient of the bulk material.[2,3] It has been shown[3,5] that in layer semiconductors, impurities or structural damage strongly broaden the exciton absorption peak, and thus drastically reduce its maximum value. In this example, at the exciton peak at 90 K, the bulk material absorption was taken as that of the pure material.[2,3] Not unexpectedly, the exciton peak, as measured by photoelectronic response, is broadened and thus reduced in amplitude because of the high defect concentration of the material (Table I) and of perturbed surface layers.

As mentioned in previous sections of this paper, InSe samples with faces parallel to the **c** axis are difficult to prepare because of the lamellar structure of the crystal; sawing and/or polishing procedures very strongly damage the crystal. Nevertheless, attempts to measure $L_\perp$ on samples cut parallel to the **c** axis were partly successful, as shown in Fig.

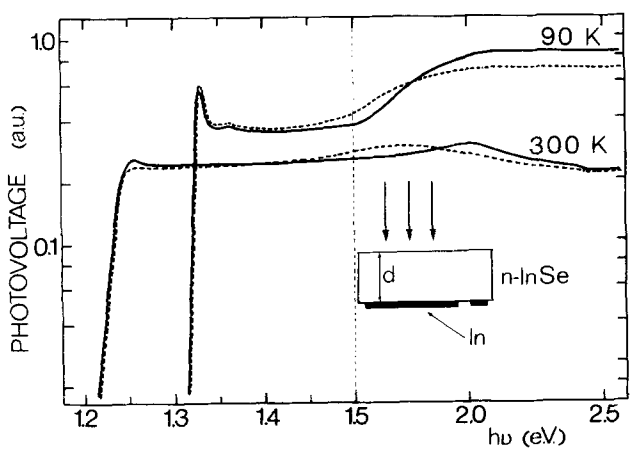

FIG. 5. Full lines: Photovoltaic spectrum (log scale) of n-type InSe (357/6) at two temperatures. Constant photon flux parallel to **c**. $d = 13\ \mu$m. Note change of abscissa scale above 1.5 eV. Dashed lines: fits with Eq. (9) with $L_\parallel = 5\ \mu$m at 300 K, and $L_\parallel = 25\ \mu$m at 90 K.

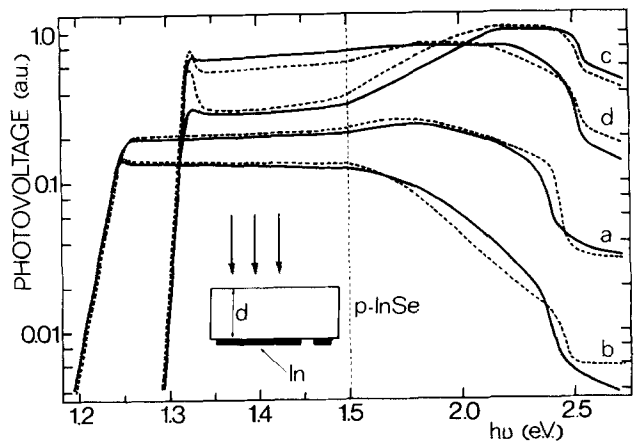

FIG. 6. Full lines: same as Fig. 5 for p-type InSe (476/61), with $d = 5.6\ \mu$m for curves a (300 K) and c (90 K), and $d = 12\ \mu$m for curves b (300 K) and d (90 K). Dashed lines: fits with Eq. (9) for a ($L_\parallel = 1\ \mu$m) and b ($L_\parallel = 1.7\ \mu$m), and Eq. (16) for c ($L_\parallel = 15\ \mu$m, $\delta = 1.5\ \mu$m) and d ($L_\parallel = 25\ \mu$m, $\delta = 2.8\ \mu$m).

7. Here the crystal was cut with a wire saw to different thicknesses. In this geometry, two different polarizations are available with light parallel (**E**||**c**) and perpendicular (**E**⊥**c**) to the **c** axis. **E**⊥**c** is the same as illumination in unpolarized light incident normal to the layers. To interpret **E**||**c** spectra, on the contrary, the parallel absorption coefficient should be used. Since the optical transition in this geometry is completely allowed,[2,3] the absorption coefficient is some two orders of magnitude higher.[3] However, its value has not been yet measured accurately enough to be used for a fit, particularly in the low-absorption region below 1.25 eV at room temperature. Qualitatively, nevertheless, the shift to low energies of the **E**||**c** spectrum with respect to the **E**⊥**c** one is representative of this difference in the absorption coefficients in the two polarizations [Fig. 7(2)]. In Fig. 7(3), the fits using Eq. (9) (dashed curves) are for $L_\perp = 85$ microns and $L_\perp = 90$ microns for samples, respectively, 220 microns and 340 microns in thickness. Diffusion length $L_\perp$ in n-type material is thus of the order of 100 microns, that is, one order of magnitude higher than $L_\parallel$, which ranges from 4 to 8 microns.

Photovoltaic measurements thus yield the same type of anisotropy along the **c** axis and perpendicular to it, as was found in photoconductivity data. The effective diffusion lengths are an order of magnitude lower, at least in n-type material. This is expected since photovoltaic diffusion lengths are limited by minority carriers properties, whereas majority carriers determine the photoconductive properties. The comparison could not be made for p-type samples since no crystals of this type with sufficient homogeneity over several hundred microns were available to do the same measurements as those of Fig. 7. The existence of perturbed layers within a few microns, at most, from the surface is confirmed by the photovoltaic spectra. Independent measurements[3-5] have shown that those damaged regions were in many instances induced by cleaving operations. This accounts for their erratic appearance in our devices where cleaving procedures are not reproducible. This type of defect should disappear if as-grown platelets or films are used (Sec. VI).

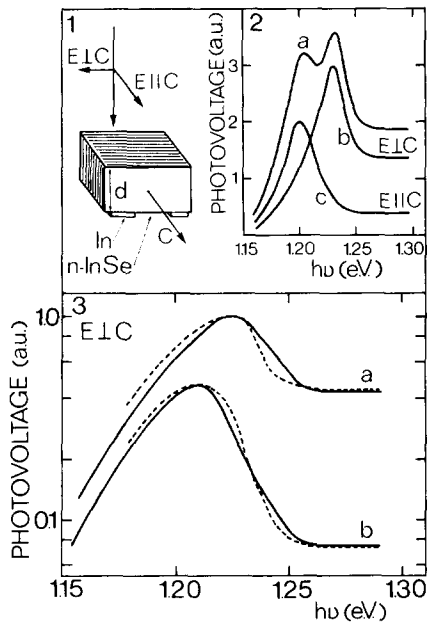

FIG. 7. Photovoltaic spectra under constant photon flux incident perpendicular to **c**. (1) Schematics of the experiment. Contacts are transverse to the layer plane. Incident light polarized parallel or perpendicular to **c**. (2) Spectra of a 110-μm-thick device: (a) unpolarized light; (b) **E**⊥**c**; (c) **E**||**c**. (3) Full lines: **E**⊥**c** spectra of (a) 220-μm-thick and (b) 340-μm-thick devices n-InSe (463/59). Dashed lines: fits with Eq. (9), using $L_\perp = 85$ μm (a) and $L_\perp = 90$ μm (b).

VI. ELECTRICAL CHARACTERISTICS AND PHOTOVOLTAIC SPECTRA OF InSe DEVICES

Several types of devices have been studied. Transverse diodes where the junction plane is parallel to the **c** axis, and where transport is in the plane of the layer, also have been fabricated and studied, but will be discussed in a separate report. Here we shall examine only planar structures with the junction plane perpendicular to the **c** axis (transport across the layers) to include the following: p-n junctions; bismuth/p-InSe, metal-semiconductor diodes; platinum/n-InSe metal-semiconductor diodes; and In_2O_3/p-InSe heterojunctions.

A. p-n junctions

As mentioned previously, p-type material reverts to n-type under thermal annealing. This provides a simple method for the fabrication of a p-n junction.[28] A temperature gradient is created in a slab of InSe by heating one face to about 500 °C by thermal contact with a heater, the other face being attached to a water-cooled copper block. The heated portion of the sample reverts to n-type and the base remains p-type. Contacts are taken on the sides of the device either with evaporated indium, or with silver paint, leaving most of the front and back surfaces exposed. For a given temperature, the profile of the junction is determined by the thickness of the sample. $J(V)$ characteristics for current density versus voltage can be expressed as

$$V = \frac{nkT}{q} \ln\left(\frac{J}{J_s} + 1\right) + JR_s , \tag{17}$$

where V is the applied voltage; n is a phenomenological factor; J is the current density across the diode; J_s is the saturation current density, and R_s is the series resistance $\times$ diode surface.

For diodes about 20 microns in thickness, unit area resistances R_s are of the order of 1 kΩ cm^2 and saturation current densities J_s between 10 and 40 μA/cm^2. Empirical factors n are high, usually close to 3. This indicates that the concentration profile is far from abrupt, with this fabrication method. Illumination from the n- or p-side of the junction gives different spectral dependence of the photovoltaic response, and this allows a check on some parameters of the device. Figure 8 shows two photovoltaic spectra for a 23-microns-thick diode. Illumination is on the p-type base (curve b) or on the n-side (curve a). Using Eq. (9), curve b can be fitted (dashed curve) with $L_n = 2$ microns and $d = 23$ microns. Using Eqs. (9), (10), and (13), curve a can then be fitted (dashed curve) with $L_p = 0.5$ microns; $L_n = 2$ mi-

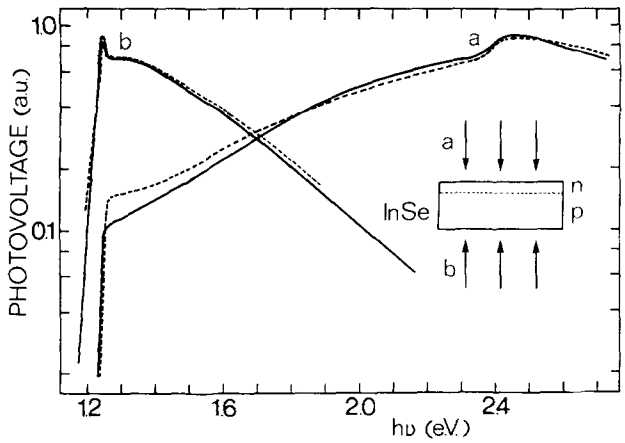

FIG. 8. Photovoltaic spectra of a p-n junction; p-InSe (393/23) is the base material (see text). Total thickness: 23 μm. Full curves: (a) illumination on the n-side; (b) illumination on the p-side. Dashed curves: (a) fit with Eqs. (9) + (10) + (13) with $L_p = 0.5\ \mu$m, $L_n = 2\ \mu$m, $d = 0.2\ \mu$m, and $w = 0.5\ \mu$m. (b) Fit with Eq. (9), $L_n = 2\ \mu$m and $d = 23\ \mu$m.

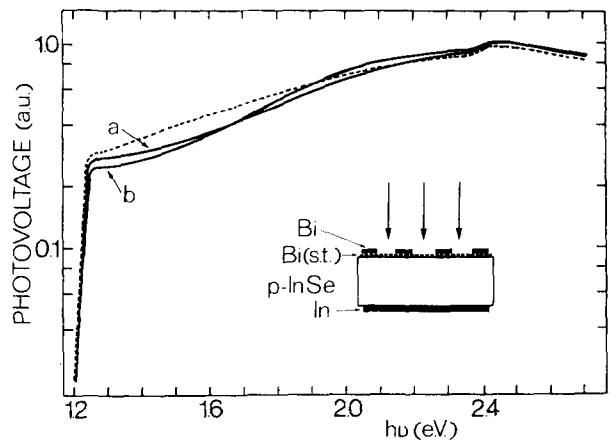

FIG. 10. Photovoltaic response of Bi/p-InSe junctions. Thicknesses are 8 μm (curve a) and 60 μm (curve b). Dashed curve: fit with Eq. (15) is insensitive to thickness: $w = 0.5\ \mu$m, $L_n = 2\ \mu$m, and $\delta = 0.05\ \mu$m.

crons; $d = 0.2$ microns, and $w = 0.5$ microns. The low value of diffusion length in the n-type region is certainly representative of its being located at the surface of the sample. This type of fit is given, principally, to demonstrate the fact that our simplifying assumptions, and, consequently, Eqs. (9), (10), and (13), are sufficient to account quantitatively for the photovoltaic behavior of a comparatively complex structure.

B. Bismuth/p-InSe junctions

Bismuth has been found to give rectifying contacts with p-type InSe. Cells were made with a semitransparent illuminated Bi electrode and an indium ohmic electrode at the back, as described in a previous paper.[28]

Electrical characteristics using Eq. (17) for a 10-micron-thick samples give R_s from 40 to 80 ohms$\times$cm^2, J_s of the order of 10 μA/cm^2, and for the best diodes of the series. In Fig. 9, a is shown the C^{-2} vs V characteristic from which[34] the depletion layer width w and barrier height V_B may be calculated, namely $w = 0.4\,\mu$ and $V_B = 0.7$ V. In this geometry, when the total thickness e of the device becomes larger than both the depletion layer and the effective diffusion length, the spectrum does not depend on e, within a constant factor. Thus Eq. (15) (dashed line) can equally be fitted to curves a and b of Fig. 10, which is the experimental photovoltaic spectra of two diodes of 8 and 60 microns thickness. The parameters of this fit are $w = 0.5$ microns, $L_n = 2$ microns, and $\delta = 0.05$ microns.

C. Platinum/n-InSe junctions

Two types of diodes have been prepared, one for illumination through the base material with the rectifying contact at the back, and the other for illumination through the semitransparent platinum electrode.

The first structure is shown in the insert in Fig. 11. Rectifying behavior is obtained with no annealing treatment. This type of structure can be used to measure diffusion lengths in the material. On Fig. 11, two photovoltaic spectra are shown, for diodes 6 and 9 microns in thickness (curves a and b). Curve fits (dashed lines) are shown with a value of 3 microns for L_p. The base material (554/116) has been made from unrefined 4N indium. This shows that even industrial-

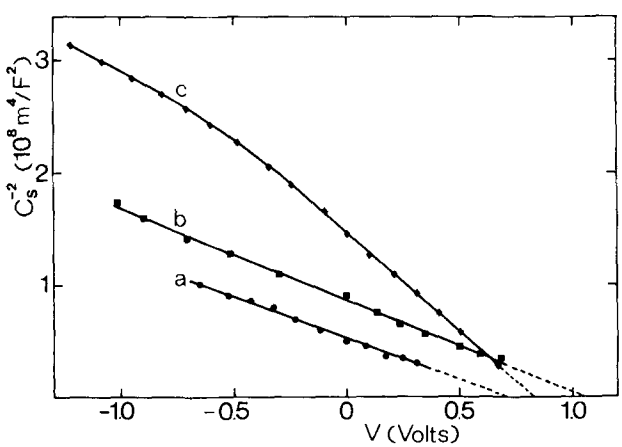

FIG. 9. Voltage-capacitance characteristics of three InSe rectifying structures: (a) Bismuth/p-InSe (393/23); (b) Platinum/n-InSe (554/116); and (c) ITO/p-InSe (561/122).

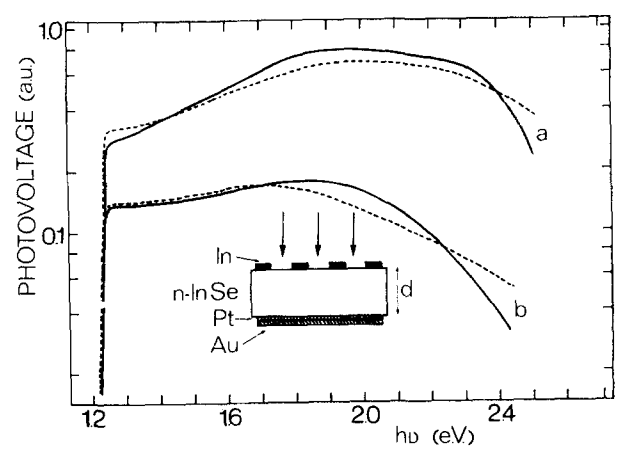

FIG. 11. Photovoltaic spectra of two Pt/n-InSe (554/116) junctions. Thicknesses are 6 μm (curve a) and 9 μm (curve b). Dashed curves: Fits with Eq. (9) for $L_p = 3\ \mu$m in both curves.

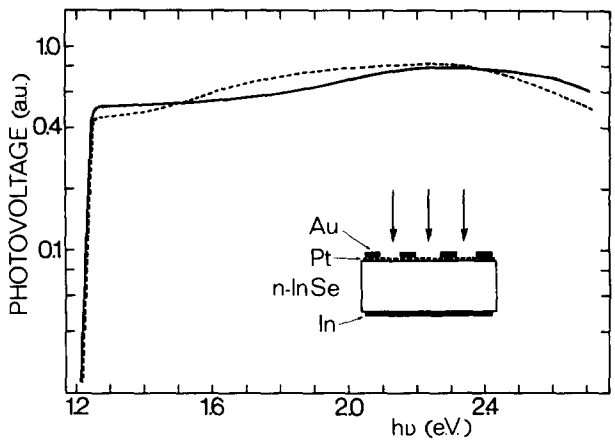

FIG. 12. Photovoltaic spectrum of a Pt/*n*-InSe (554/116) junction. Illumination is on the barrier side (opposite to Fig. 11). Thickness: 10 μm. Dashed curve: fit with Eq. 15: $w = 0.6\,\mu$m, $L_p = 8\,\mu$m, $\delta = 0.1\,\mu$m.

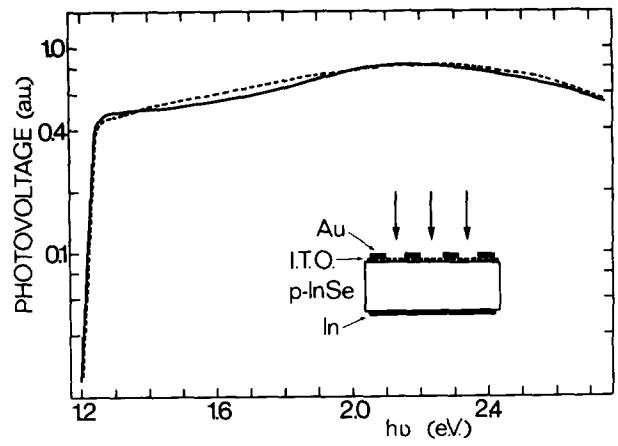

FIG. 13. Photovoltaic response of an ITO/*p*-InSe (561/122) junction. Thickness: 10 microns. Dashed curve: fit with Eq. (15). Reflectivity of ITO included (see text) $w = 1\,\mu$m, $L_n = 7\,\mu$m, $\delta = 0.1\,\mu$m, and $d_1 = 0.06\,\mu$m.

grade material still exhibits diffusion lengths which are compatible with solar conversion applications.

The second type of structure is shown in the insert of Fig. 12. Here also, no heat treatment is necessary to get rectification with the semitransparent platinum electrode. A fit with Eq. (17) of the experimental $J(V)$ characteristics gives $R_s < 2$ ohm$\times$cm^2, $J_s \sim 3\,\mu$A/cm^2, and $n \sim 2$. The capacitance-voltage characteristic of Fig. 9(b) gives the following parameters for the barrier: $w = 0.6$ microns and $V_B = 1.05$ V. Figure 12 shows the photovoltaic spectrum of one of those diodes, the solar efficiency of which was among the highest (Pt-N2-30 in Table III). The dashed curve was calculated along Eq. (15) with $w = 0.6$ microns, $L_p = 8$ microns, and $\delta = 0.1$ microns. Comparison of this value of L_p with those found from the fit in Fig. 11 (3 microns) shows that for the same ingot (554/116), effective diffusion lengths parallel to c may vary considerably from one end of the crystal to the other. Clearly, high efficiency structures came from the material with comparatively high diffusion lengths.

D. ITO/*p*-InSe heterojunctions

ITO/*p*-InSe heterojunctions have been fabricated by reactive dc sputtering in an oxygen atmosphere from a 90% In: 10% Sn cathode. The temperature of the substrate during the process was never more then 300 °C, that is, somewhat below the temperature required for switching to *n*-type. The material ITO acts as the *n*-side of the junction and as a good antireflecting coating, since its index ($n_1 = 2$)[35–38] is close to the ideal value ($n = 1.7$) for InSe ($n \sim 3$).[3]

The optimum thickness can be derived by maximizing

TABLE III. Electrical and photoelectrical performance of InSe devices. *Column 1*: PN are *p-n* junctions; BP, bismuth/*p*-InSe; Pt N, platinum/*n*-InSe; and IP, ITO/*p*-InSe. *Column 5*: Specific series resistance: series resistance multiplied by cell area. *Column 7*: Empirical quality factor of the junction, *n*, in Eq. (17). *Column 8*: Series PN and BP are studied under 60 mW/cm^2 sun light; PT N and IP under simulated conditions. *Column 9*: Bismuth electrodes transmittancy varies from 20% to 30% over the solar spectrum.

1	2	3	4	5	6	7	8	9	10	11	12	13
				Electrical parameters			Photoelectrical parameters under solar conditions					
Diode number	InSe substrate	Active surface mm^2	Thickness μm	R_s Ω cm^2	J_s μA/cm^2	n	Φ mW/cm^2	Transmitance electrode %	J_{sc} mA/cm^2	V_{oc} V	f	η %
PN 12	393/23	0.5	20	20	13	3	60	...	4.7	0.34	0.28	0.7
PN 16	393/23	1	19	200	9	3	60	...	3.9	0.38	0.38	0.9
BP 7-2	393/23	1.4	7	35	9	2.2	60	20-30	4.9	0.30	0.35	0.8
BP 9-2	393/23	3	8	75	23	1.8	60	20-30	5.3	0.34	0.37	1.1
BP 10-2	507/81	2.4	12	12	180	3	60	20-30	5.4	0.21	0.28	0.5
BP 10-3	507/81	1.8	9	9	25	1.7	60	20-30	5.1	0.24	0.45	0.9
Pt N2-1	554/116	1.4	2	0.1	0.7	2.4	100	70	14.8	0.58	0.62	5.3
Pt N2-12	554/116	3.2	7	0.1	42	3.4	100	70	14.4	0.51	0.55	3.8
Pt N2-20	554/116	9.1	20	0.1	14	3.2	100	70	11.3	0.54	0.45	3.3
Pt N2-30	554/116	10	10	0.1	4	2.7	80	70	13.3	0.56	0.61	5.7
Pt N4-1	674/208	9.3	19	...	13	2	100	50	12.7	0.60	0.50	3.7
IP 1-1	561/112	10	10	...	...	...	100	95	26.0	0.33	0.37	3.2
IP 2-1	561/112	6	13	7	24	2.2	100	95	25.5	0.40	0.38	3.8

the solar efficiency values, with the formulae given in the next section. Depending on the thickness of the device and effective diffusion length, the optimum thickness for AM1 spectrum is between 600 and 700 Å.

Typical electrical characteristics of these diodes can be fitted with Eq. (17). For approximately 20-micron-thick devices, the parameters of the fit are $R_s \sim 50$ ohm cm^2, $n \sim 1.6$, and $J_s \sim 100\ \mu$A/cm^2. From $C(V)$ characteristics (Fig. 9c), barrier parameters are $w = 0.8$ microns and $V_B = 0.8$ V.

Figure 13 shows the photovoltaic spectrum of a 10-micron-thick cell with a comparatively high efficiency (IP1-1 in Table III). The ITO layer is 600-Å thick. The dashed curve is calculated from Eq. (15) multiplied by a factor $1 - R/1 - r$, with r the reflectivity of InSe[3] and R the reflectivity of the device. The quantity R is given by

$$R = \frac{R_1^2 + R_2^2 + 2R_1R_2\cos\theta}{1 + R_1^2R_2^2 + 2R_1R_2\cos\theta}, \tag{18}$$

where

$$R_1 = \frac{n_1 - 1}{n_1 + 1},$$

$$R_2 = \frac{n_2 - n_1}{n_2 + n_1},$$

$$\theta = \frac{2\pi n_1 d_1}{\lambda},$$

and n_1 is the refractive index of ITO taken as 2; n_2 is the refractive index of InSe from Ref. 3; d_1 is the thickness of the ITO layer, and λ is the wavelength of incident light. The parameters of the fit were $w = 1$ micron, $L_n = 7$ microns, $\delta = 0.1$ micron, and $d_1 = 0.06$ microns. In this material (561/122), the diffusion length was somewhat higher than in most p-type material, which accounts for its higher efficiency.

Examination of the results presented in this section shows that InSe may be used for a variety of possible devices for solar energy conversion. The optical and phototransport properties are now sufficiently investigated so that the photovoltaic response can be quantitatively interpreted over all the useful part of the solar spectrum (1.25 to 2.8 eV). Barriers can be as high as 1 V, which is close enough to the band gap. Clearly among the devices examined here, Pt/n-InSe stands out with its low saturation current and high potential barrier. Understandably, these devices have shown the highest efficiency up to now, as shown in the next section.

VI. SOLAR EFFICIENCY

Efficiencies of the various devices described here have been measured under real and simulated solar irradiation, with reference to calibrated silicon diodes. Figures 14 and 15 shows examples of $J(V)$ characteristics in the fourth quadrant of devices of each type. In Fig. 14, a solar flux of 60 mW/cm^2 was used. Results in Fig. 15 are for 100 mW/cm^2 of simulated AM1 irradiation. Table III sums up the results of efficiency data, as well as relevant parameters which determine the efficiency. The highest observed external efficiency was 6% for diode Pt N2-30 under 100 mW/cm^2 (5.7% under 80 mW/cm^2, see Table III). Electrical characteristics (V_B and J_s) of platinum/n-InSe devices clearly give the best efficiencies with a fill factor of 0.62 and V_{oc} of 0.6 V. Considerable improvement should come from increase of J_{sc} which is rather far from the maximum value, due in part to limited transmittancies of the platinum front electrodes in Pt/n-InSe diodes. Cells of ITO/p-InSe gave $J_{sc} = 26$ mA/cm^2 under 100 mW/cm^2 irradiation as a result of the better optical quality of the ITO coating. This does not lead to an increase of the efficiency, however, because of poor electrical quality of the p-InSe and of the low open-circuit voltage for this type of barrier. Nevertheless, it does show that InSe can yield close to maximum optical collection efficiency over the solar spectrum. In order to increase the overall external efficiency, several other limiting factors should be taken into account.

Potential barriers of over 1 V, which we observed on Pt/n-InSe, may not be the highest possible for a semiconductor with a 1.3-eV gap. Nevertheless, it is close enough that only modest increases should be expected. On the contrary, V_{oc}'s of 0.6 V are certainly not an upper limit, but depend upon the electrical characteristics with most improvement expected for p-type material. Efficiency also depends on the fill factor

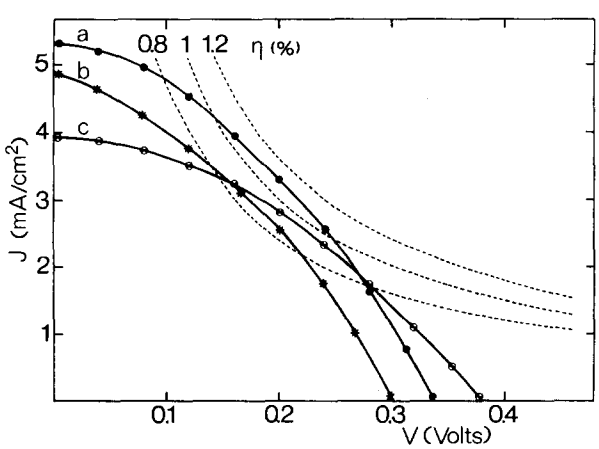

FIG. 14. Current-voltage characteristics of three cells under 60 mW/cm^2 sunlight. (a) BP 9-2, (b) BP 7-2, (c) PN 16.

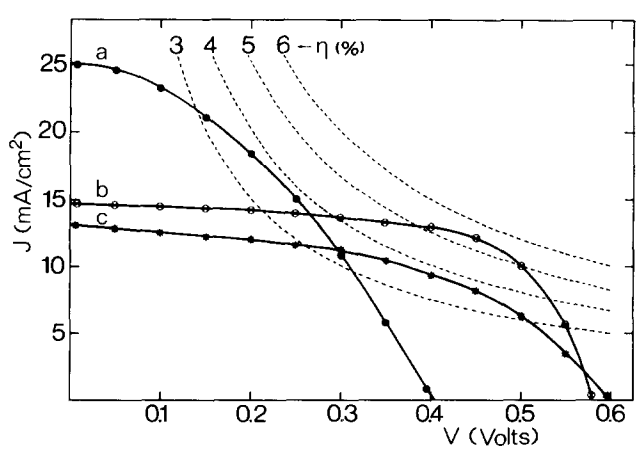

FIG. 15. Current-voltage characteristics of three cells under simulated AM1 sun (100 mW/cm^2). (a) IP 2-1, (b) Pt N2-1, (c) Pt N4-1.

(through the series resistance), and also on the limiting saturation current density which has never been found lower than 0.1 μA/cm^2. Series resistances certainly can be decreased by orders of magnitude by improving the material, especially p-type. This will involve more effort in crystal growing procedures. The high values of the n-factor do point to recombination occurring within the depletion layer, both in the bulk and at the surface. It is possible that cleaving procedures that we use introduce interlayer stacking faults which should disappear in as-grown thin films.

One improvement that can be effected immediately is the optimization of J_{sc}. This factor depends on the geometry of the cell (front or back illumination), the thickness of the antireflecting layer, the thickness of the device, and the phototransport characteristics of the material.

The solar flux spectrum being $\Phi(E)$ at the surface of the sample (here, not corrected for reflectivity losses), we have:

$$J_{sc} = \int_{1.24\ \text{eV}}^{4\ \text{eV}} q \frac{\Phi(E)}{E} [1 - R(E,d_1)] \eta[\alpha(E),e,L,w,\delta] dE , \tag{19}$$

where $\Phi(E)$ is the solar energy flux density in mW/cm^2 eV, $R(E,d_1)$ is the reflectivity of the ITO/InSe surface [Eq. (18)], $\eta[\alpha(E),e,L,w,\delta]$ is the quantum efficiency of the device, and E is the photon energy.

In the calculation, the contribution of light reflected from the back surface is taken into account by assuming the metal electrodes to be totally reflecting. When the barrier is on the illuminated surface, we have

$$\eta = \exp(-\alpha\delta) - \exp(-\alpha w) + \exp(-2\alpha e)[\exp(\alpha w) - \exp(\alpha\delta)] + \frac{\alpha L}{\alpha L + 1}\left[\exp(-\alpha w) - \exp\left(-\alpha e - \frac{d-w}{L}\right)\right] + \exp(-\alpha e)\frac{\alpha L}{\alpha L - 1}\left[\exp\left(\frac{w-e}{L}\right) - \exp(-\alpha e + \alpha w)\right] . \tag{20}$$

When the rectifying electrode is at the back, we have (in this case, we take $\delta = 0$):

$$\eta = 2\exp(-\alpha e)\sinh(\alpha w) + \frac{\alpha L}{\alpha L - 1}\left[\exp\left(\frac{w-e}{L}\right) - \exp(-\alpha e + \alpha w)\right] + \exp(-\alpha e)\frac{\alpha L}{\alpha L + 1}\left[\exp(-\alpha w) - \exp(-\alpha e)\exp\left(\frac{w-e}{L}\right)\right] . \tag{21}$$

Results shown in Figs. 16 and 17 have been calculated with the preceding equations for $w = 1$ micron and $d_1 = 0.065$ microns. This thickness minimizes reflection losses over the solar spectrum for InSe. With diffusion lengths of 8 microns, short-circuit currents of 31 mA/cm^2 can be expected, with the junction at the front of the device. Insert 1 in Fig. 16 shows the influence of the antireflecting layer thickness upon J_{sc}. Insert 2 in Fig. 16 shows the influence of the perturbed surface layer thickness upon J_{sc}. This calculation is consistent with the fits to our photovoltaic spectra and with efficiency measurements. Indeed, with $L \sim 8\mu$, $w \sim 1\mu$, $d_1 \sim 0.07\mu$, and $\delta \sim 0.1\mu$, short-circuit current density must be of the order of 25 mA/cm^2, which occurs for our ITO/p-InSe cells.

Diodes with high short-circuit current density (IP series) are reported in Table III. The main drawback with this type of devices is that it implies using p-type material. This type of material is less reproducible than n-type InSe, and its phototransport properties are far from satisfactory. The other type of diodes, with the junction at the back, can be made from n-InSe, short-circuit current densities being some 15%

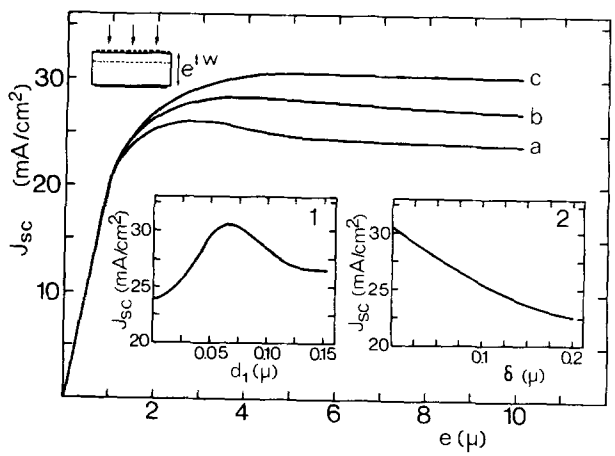

FIG. 16. Calculated short-circuit current density under 100 mW/cm^2 AM1 of an ITO/InSe cell, illuminated on the ITO side: $w = 1$ μm, $n_1 = 2$, $d_1 = 0.065$ μm. Back surface totally reflecting. e is the total thickness of the InSe base. Curve (a): $L_{\parallel} = 2\mu$m; curve (b): $L_{\parallel} = 4\mu$m; curve (c): $L_{\parallel} = 8\mu$m. Insert 1: Influence of d_1 (antireflecting electrode thickness) for $e = 5\mu$m and $L_{\parallel} = 8$ μm. Insert 2: Influence of the thickness of the perturbed surface layer δ, for $L_{\parallel} = 8$ μm, $e = 5$ μm, and $d_1 = 0.065$ μm.

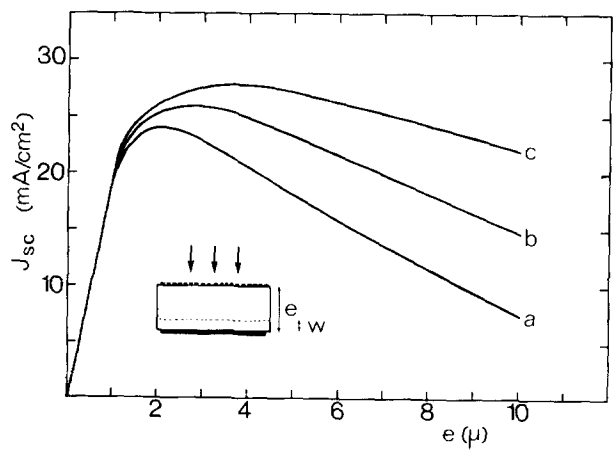

FIG. 17. Same calculation as Fig. 16. Same conditions, except the barrier is on the unilluminated side and diffusion lengths are $L_{\parallel} = 4$ μm (a), $L_{\parallel} = 8$ μm (b), and $L_{\parallel} = 16$ μm (c).

lower, and the thickness of the device becoming a sensitive parameter, as shown in Fig. 17. Optimum thickness would range between 2 and 3 microns.

VII. CONCLUSION

A constant factor in the transport properties and photoelectronic behavior of layered compounds is their large anisotropy with respect to the **c** axis. This feature dominates over the intrinsic properties of bulk material and leads to unique effects. These are due to the presence of two-dimensional defects (faults and/or precipitates), and thus a better understanding of this type of defect is of prime interest to improve devices using InSe or other layer compounds.

Nevertheless, effective lifetimes or diffusion lengths for carrier transit parallel and perpendicular to the **c** axis can be utilized to give exact and quantitative fits to the photoconductivity or photovoltage spectra, for all devices and configurations presented in this work. This was a main point of this paper since it was all but evident that quantities such as diffusion lengths or mobilities, which were derived from equations describing three-dimensional crystals, would not apply to highly anisotropic solids.

A third point which we demonstrate here is the feasibility of a variety of photovoltaic devices which can be readily fabricated from InSe. In those devices, as mentioned above, the shape of the photovoltaic response can be accurately analyzed. Detailed explanation of the electrical properties of the rectifying structures, however, remains an open question, mainly because of poor knowledge of impurity levels in the bulk material, and of the origin of potential barriers with the metal electrodes.

From the point of view of solar energy conversion, therefore, the devices that we describe here are certainly in a primitive stage compared with conservative expectations. Many of the undesirable features of InSe may actually lead to unique and interesting behavior once a better control over interlayer defects is achieved. For instance, the tendency of impurities towards segregation within the crystal leaves strata of pure high-quality material, even with unrefined elements. In other types of applications, such as MOS-FET devices, for instance, one might be able to take advantage in principle, of the very high conductivity anisotropy, to maintain parallel current lines between the source and the drain under load.

As regards applications to solar energy conversion, InSe should be regarded as a possible candidate for thin-film cells because of its high mechanical flexibility. Those films might be fabricated by continuous deposition of thin monocrystal in the substrate plane and *not* perpendicular to it, as in the case of three-dimensionally bonded semiconductors.

[1]A. Chevy, A. Kuhn, and M. S. Martin, J. Cryst. Growth **38**, 118 (1977).
[2]M. V. Andriyashik, M. Yu. Sakhnovskii, V. B. Timofeev, and A. S. Yakimova, Phys. Status Solidi **28**, 277 (1968).
[3]N. Piccioli, R. Le Toullec, F. Bertrand, and J. C. Chervin, J. Phys. **42**, 1129 (1981).
[4]J. Camassel, P. Merle, H. Mathieu, and A. Chevy, Phys. Rev. B. **17**, 4718 (1978).
[5]R. Le Toullec and N. Piccioli (private communication).
[6]J. V. Canny and R. B. Murray, J. Phys. C. **10**, 1211 (1977).
[7]A. Bourdon, A. Chevy, and J. M. Besson, *Proceedings of the 14th International Conference of Physics of Semiconductors, Edinburgh* [I.O.P. Conf. Ser. **43**), 1371 (1978)].
[8]R. H. Williams, J. V. Canny, R. B. Murray, L. Ley, and P. C. Kemeny, J. Phys. C **10**, 1233 (1977).
[9]P. K. Larsen, S. Chiang, and N. V. Smith, Phys. Rev. B **15**, 3200 (1977).
[10]G. Ottaviani, C. Canali, F. Nava, Ph. Schmid, E. Mooser, R. Minder, and I. Zschokke, Solid State Commun. **14**, 933 (1974).
[11]K. Maschke and Schmid, Phys. Rev. B **12**, 4312 (1975).
[12]J. J. Forney and K. Maschke, Nuovo Cimento B **38**, 418 (1977).
[13]S. M. Ryvkin, JETP Lett. **18**, 221 (1973).
[14]S. M. Ryvkin, Sov. Phys. Semicond. **8**, 237 (1974).
[15]A. Sh. Abdinov, A. G. Kyazim-Zade, and A. A. Akumedov, Sov. Phys. Semicond. **11**, 227 (1977).
[16]R. W. Damon and R. W. Redington, Phys. Rev. **96**, 1498 (1954).
[17]S. M. Atakishiev and G. A. Akhundov, Phys. Status Solidi **32**, K33 (1969).
[18]A. S. Abdinov and A. G. Kiazym-Zade, Sov. Phys. Semicond. **9**, 1113 (1976).
[19]A. S. Abdinov and A. G. Kiazym-Zade, Sov. Phys. Semicond. **9**, 1290 (1976).
[20]A. S. Abdinov and A. G. Kiazim-Zade, Sov. Phys. Semicond. **9**, 1537 (1976).
[21]P. I. Voronyuk, A. S. Yakimova, and Z. D. Kovalyuk, Izv. Fiz. **7**, 120 (1970).
[22]C. Clemen, X. I. Saldana, P. Munz, and E. Bucher, Phys. Status Solidi A **49**, 437 (1978).
[23]A. I. Malik, V. B. Baranyuk, and Z. D. Kovalyuk, Sov. Phys. Semicond. **14**, 241 (1980).
[24]V. B. Baranyuk, A. I. Malik, V. A. Manasson, and Z. D. Kovalyuk, Sov. Phys. Semicond. **13**, 4 (1979).
[25]V. L. Bakumenko, Z. D. Kovalyuk, L. N. Kurbatov, U. G. Tagaev, and V. F. Chishko, Sov. Phys. Semicond. **12**, 216 (1977).
[26]G. B. Abdullaev, Z. A. Iskenderzade, E. A. Dzhafarova, V. I. Tagirov, A. A. Agasiev, M. A. Sobeikh, V. M. Salmanov, and I. D. Yaroshetskii, Sov. Phys. Semicond. **12**, 1354 (1978).
[27]A. Segura, J. M. Besson, A. Chevy, and M. S. Martin, Il Nuovo Cimento B **38**, 345 (1977).
[28]A. Segura, J. P. Guesdon, J. M. Besson, and A. Chevy, Rev. Phys. Appl. **14**, 253 (1979).
[29]A. Segura, A. Chevy, J. P. Guesdon, and J. M. Besson, Sol. Energy Mater. **2**, 159 (1980).
[30]T. Matsushita, T. T. Nang, M. Okuda, A. Suzuki, and S. Yoko Ta, Jpn. J. Appl. Phys. **15**, 901 (1976).
[31]K. Ando and A. Katsui, Thin Solid Films **69**, L5 (1980).
[32]A. Chevy, A. Gouskov, and J. M. Besson, J. Cryst. Growth **43**, 756 (1978).
[33]J. C. Portal, R. J. Nicholas, E. Kress-Rogers, A. Chevy, J. M. Besson, J. Galibert, and P. Perrier, *Proceedings of the 15th International Conference of Physics of Semiconductors, Kyoto, 1980* [J. Phys. Soc. Jpn. **49(A)**, 879 (1980)].
[34]S. M. Sze, *Physics of Semiconductor Devices* (Wiley, New York, 1969).
[35]D. B. Fraser and H. D. Cook, J. Electrochem. Soc. **119**, 1368 (1972).
[36]H. K. Mueller, Phys. Status Solidi **27**, 723 (1968).
[37]C. E. Wickersham and J. E. Greene, Phys. Status Solidi **47**, 329 (1978).
[38]J. C. Fan and F. J. Bachner, J. Electrochem. Soc. **122**, 1719 (1975).